Probe-assisted depopulation pumping in low-pressure alkali-metal vapor cells for magnetometry

M. E. Limes [*,†], J. Smoot, J. Perez, J. Freeman, C. Amano-Dolan, and D. Peters
National Security Institute, Virginia Tech, Blacksburg, Virginia 24061, USA

W. Lee
Department of Physics, Harvard University, Cambridge, Massachusetts 02138, USA

(Received 5 November 2025; accepted 9 February 2026; published 2 March 2026)

For precision atomic magnetometry, inert buffer gas is included in alkali-metal vapor cells to significantly broaden hyperfine transitions, which facilitates optical pumping and reduces diffusive relaxation, while also providing nonradiative excited-state quenching. We show low-buffer gas pressure (below 50 Torr) alkali-metal vapor cells with resolved hyperfine manifolds can also yield high-performance magnetometers. For high polarization in ^{87}Rb, we optically pump $F = 2$ states with narrow linewidth σ_+ light, while tuning a probe beam to depopulate $F = 1$ states ($\Delta\nu = 6.8$ GHz from $F = 2$). The probe tuning then also provides $F = 2$ detection with high optical rotation and low probe broadening; we demonstrate top-bottom gradiometry, within a single 25-Torr, 0.5-cm^{3}cell, that yields an Earth's field free-precession magnetometer sensitivity of 18 fT/$\sqrt{\text{Hz}}$ with a 1 kHz bandwidth, as well as an RF magnetometer sensitivity of 12 fT/$\sqrt{\text{Hz}}$ in a small band about 110 kHz.

DOI: 10.1103/pbrt-m6q3

Warm alkali-metal vapor systems rival superconducting quantum interference devices (SQUIDs) for the world's most sensitive magnetic field measurements [1]. Warm-atom systems hold several advantages for portable sensing, such as heated operation, rather than the cryogenic cooling and dewars required for SQUIDs. Miniature, high-performance atomic sensors are quickly becoming mature, aided by key innovations such as single-mode vertical-cavity surface-emitting lasers (VCSELs) and anodically bonded cells [2]. Commercial near-zero-field atomic magnetometers show great promise for magnetically shielded magnetoencephalography (MEG) studies involving minor motion [3–5], using the popular spin-exchange relaxation-free (SERF) atomic magnetometer [6]. However, SERF, and other styles of alkali-metal magnetometers such as free-precession scalar, lose significant sensitivity at the Earth's field and above due to effects that result from hyperfine coupling within the alkali-metal atoms, such as spin-exchange relaxation [7] and heading errors [8,9].

Portable free-precession atomic magnetometers have sufficient performance unshielded in the Earth's field to detect MEG signals [10,11], in addition to other various applications, due to their high dynamic range and linearity, resulting from frequency measurements ω of spins precessing due to a total magnetic field B. Here, calibration is provided by the gyromagnetic ratio $\gamma = \omega/B$ [12–15], rather than the voltage/field measurements of SERF and rf [16] sensors that require frequent calibration. Scalar magnetometers also demonstrate high performance within magnetic shielding, comparable to other precision modalities [17–19]. As such, there is high interest in developing methods to improve scalar magnetometer functionality [20], including introducing field modulations for vector sensing [21–23].

For precision magnetometry, it is common that sufficient buffer gas (above 50 Torr N_2) is added to vapor cells for optical pumping efficiency, and slowing diffusive wall relaxation [24–29]. Here, absorption-line broadening is done for efficiency of both broad and narrow linewidth semiconductor lasers; for the former, broadening causes more absorption line overlap with a wide laser spectrum, and the latter so that all ground hyperfine states can be pumped. Trade-offs of broadening include lowered in-peak absorption efficiency, and lower maximum optical rotation by an incident linearly polarized probe beam [30]. We show careful probe tuning can assist optical pumping in low buffer gas pressure vapor cells, leading to high polarizations, while retaining large optical rotation for detection. We give a basic theory, and experimentally demonstrate high sensitivity and high bandwidth for scalar and RF magnetometers. Probe-assisted depopulation pumping also suppresses hyperfine coupling effects, such as heading error, and improves tolerance to large fields and inhomogeneous dephasing from magnetic gradients, important for a variety of applications of high-performance atomic magnetometry, such as MEG, magnetic navigation [31], and neutron electric dipole moment (nEDM) searches [32].

Scalar free-precession magnetometers are best operated by polarizing alkali-metal atoms to unity into an edge state, maximizing the signal-to-noise ratio (SNR) and providing T_2 extension by suppressing spin-exchange relaxation [8,18]. Whether optical pumping occurs pulsed in a plane transverse to the measured scalar magnetic field B_0, or is done longitudinally followed with a $\pi/2$ tipping pulse, a resulting transverse spin polarization will freely precess about a total field B_0,

[*]Present address: Bradley Department of Electrical and Computer Engineering, Virginia Tech, Blacksburg, Virginia 24061, USA.
[†]Contact author: limes.mark@gmail.com

where light shifts are avoided with no pump laser during detection periods. The probe is tuned to maximize sensitivity, which is a trade-off of maximizing initial optical rotation while reducing probe broadening until it competes with the next largest rate (typically spin-exchange or wall relaxation). Increasing T_2 is beneficial to optimal sensitivity by roughly the measurement time T, which can be seen by converting the Cramér-Rao lower bound (CRLB) estimate of frequency noise [33,34] to a field sensitivity,

$$\delta B = \frac{\sqrt{12C}}{2\pi\gamma(A/\rho)T^{3/2}\sqrt{\mathrm{BW}}}\left(\frac{\mathrm{T}}{\sqrt{\mathrm{Hz}}}\right), \tag{1}$$

with SNR A/ρ, integration time T, pulsed sensor bandwidth $\mathrm{BW} = 1/2T_{\mathrm{rep}}$, and C dependent on T_2 and T. Over a decay period, the average frequency of spin precession is proportional to the magnetic field through the low-field, strong hyperfine coupling gyromagnetic ratio γ (e.g., ^{87}Rb, $\gamma \approx 7$ GHz/T). To minimize Eq. (1), a single shot should last $\sim 2T_2$ [35]. Measurements are repeated every T_{rep} for a flat magnetometer bandwidth BW, with caveats—there are amplitude corrections required at higher in-band frequencies, and significant aliasing of out-of-band frequencies [36]. Artificially higher bandwidth magnetometers may be made by decreasing fitting windows, at a sensitivity loss linearly proportional to increasing bandwidth [37,38].

At low buffer gas pressures for ^{87}Rb (below 100 Torr), $F = 2$ and $F = 1$ ground states can be addressed separately by narrow linewidth light [39,40]. For this study, we are in a regime where narrow linewidth σ_+ pump light is efficient, but can only address either $F = 2$ or $F = 1$ at a given time. As shown by the assisted ($\star$) regime in Fig. 1, an additional laser, such as a linearly polarized σ_0 transverse probe, can be tuned to simultaneously drive transitions from $F = 1$. While the σ_+ pump drives $F = 2$ states to the $m_F = 2$ edge state, an additional depopulation of $F = 1$ can achieve a maximum $\times 1.6$ enhancement in edge-stage polarization. After a pumping period, the linearly polarized probe tuned to $F = 1$ transitions is already conveniently detuned from the highly polarized $F = 2$ manifold by the $\Delta\nu = 6.8$ GHz hyperfine splitting, to provide high optical rotation with low magnetic linewidth probe broadening. For magnetometry, there are several advantages of probe-assisted depopulation pumping over high buffer gas operation, where the absorption lines of the hyperfine manifolds overlap. During detection, the probe also continuously depopulates $F = 1$, suppressing spin-exchange relaxation at high polarizations even in Earth-scale fields. Here, we are wall relaxation and probe broadening limited. Also, $F = 1$ contributes zero optical rotation, thus no frequency chirp from fast-decaying $F = 1$ states (precession ~ 1 kHz difference from $F = 2$ at 44 μT), leaving only nonlinear Zeeman heading error effects [8,41].

A model for probe-assisted depopulation pumping for free-precession magnetometry is made using the absorption cross section $\sigma = \pi r_e c f\,\mathrm{Re}[V(\nu)]$ and optical rotation $\phi = l r_e c f n P_x\,\mathrm{Im}[V(\nu)]/2$, with classical electron radius r_e, speed of light c, D_1 oscillator strength $f = 0.34$, path length l, alkali-metal number density n, and P_x is polarization along the probe axis. We use Voigt profiles, as Doppler broadening $\Gamma_G = 0.57$ GHz is comparable to buffer-gas broadening

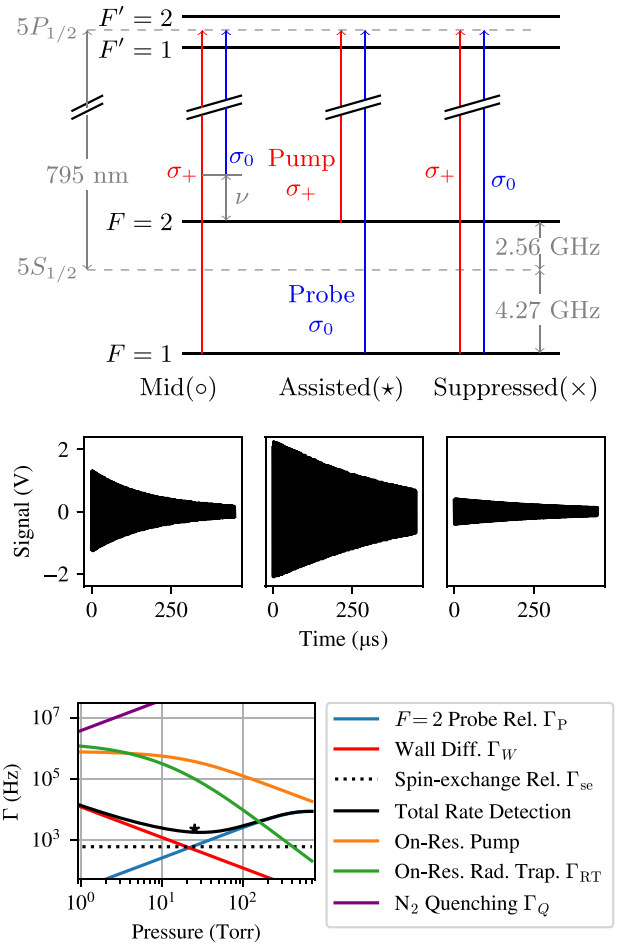

FIG. 1. Top: Grotrian diagram for several regimes, along with representative data. Bottom: Dominant rates for probe-assisted depopulation pumping; N_2 quenching overcomes radiative trapping, with ($\star$) denoting experimental conditions being wall-relaxation and probe-broadening limited.

$\Gamma_L \approx 18p/p_0$ GHz, with buffer gas pressure p, and $p_0 = 760$ Torr. For narrow laser linewidths, pumping rates are $\Gamma_P = \Phi\sigma$, with photon flux $\Phi = I_0/h\nu$. Small cells with very low buffer gas pressures (e.g., $\ll 1$ cm^3, 10 Torr) have large diffusive relaxation to walls, depolarizing atoms that can then contribute to radiation trapping [42]. The radiation trapping rate is estimated by $\Gamma_{RT} = K(M-1)f_{spon}\Gamma_P/2$ given in Ref. [42], where at 100 °C, $K = 0.12$, and $M = 28$ is the average number of times a photon is emitted before escaping the cell. We find a wide range of N_2 pressures are sufficient to provide nonradiative quenching, with greater than 10 MHz quenching rates Γ_Q, compared to on-resonance ~ 0.5 MHz pumping/radiation trapping rates. For diffusive wall relaxation, we use $\Gamma_W = [(\pi/L)^2 + (\mu/R)^2]D_0 p_0/p$, with L and R the cell length and radius, and diffusion coefficient D_0 for Rb in buffer gas [28]. Shown in Fig. 1, ~ 20 Torr maximizes coherence time for probe-assisted depopulation pumping for our conditions; we also project a optimum sensitivity at this pressure of 8 fT/$\sqrt{\mathrm{Hz}}$ with 1.2 kHz bandwidth. Compare to high buffer gas broadening, where Voigt profiles are replaced by complex Lorentzians and maximum optical rotation occurs with tuning $\nu_{opt} = \Gamma_L/2$; we also find optimal sensitivity δB

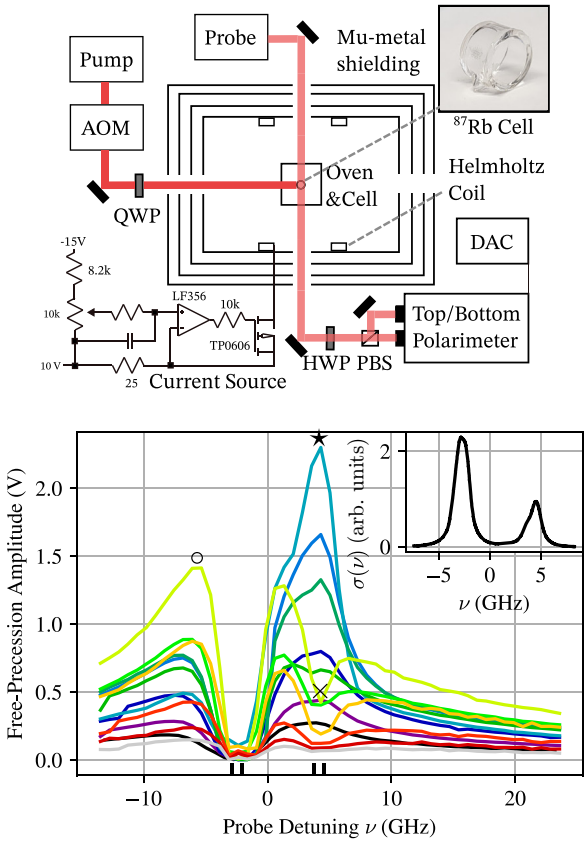

FIG. 2. Top: Schematic of σ_+ light optically pumping a ^{87}Rb cell along a 44 μT field. After pumping periods, tipping pulses are applied, and spin precession is detected by optical rotation of a linearly polarized probe. Bottom: For a 25-Torr buffer gas ^{87}Rb cell at 90 °C, the scalar magnetometer amplitude responds to variation of probe and pump wavelengths. The probe detuning is shown along the x axis, with pump detuning plotted from violet to red (low to high ν) in steps of 1.46 GHz. Labeled are mid (○), assisted (⋆), and suppressed (×) regimes, and a guide along the x axis $F \to F' : 2 \to 1, 2 \to 2, 1 \to 1, 1 \to 1$. Inset: Linearly polarized probe absorption cross section $\sigma(\nu)$.

increases as Γ_L when probe broadening Γ_P competes with buffer gas pressure independent rates Γ_{NP}, and bandwidth lowers with $1/\Gamma_L$.

For experiments, we use a ^{87}Rb vapor cell with two optical flats separated by 6 mm internal dimension and inner 10 mm diameter (0.47 cm^3), with 25 Torr of buffer gas, ratio 3:2 Ar:N_2. The cell is heated in a boron nitride oven with manganin wire driven by 80 kHz cw. Both the pump and probe are Photodigm 795-nm lasers with 0.5 MHz linewidth. We use 5–10 mW peak from each laser incident on the vapor cell. In Fig. 2, the pump light is fed into a InterAction Corporation Acousto-Optic Modulator (AOM), and circularly polarized by a quarter-wave plate (QWP). The probe beam passes through the cell's optical flats, and into a half-wave plate (HWP) and balanced polarimeter with a polarizing beamsplitter cube (PBS), and a custom top-bottom polarimeter using split photodiodes. When balanced, 1 mW of light hits each of the four photodiode regions. The photon-shot-noise-limited signal is digitized with a National Instruments PXI-5922 card. To simulate the Earth's field within magnetic shielding, a 40-turn Helmholtz coil is driven by a Libbrecht-Hall circuit [43]. The bias field and pump are applied along the cylinder axis, with the probe transverse. After pumping, a resonant $\pi/2$ pulse is applied by a 4-cm-sq. Helmholtz coil, placing spins on the transverse plane.

For a demonstration of probe-assisted depopulation pumping, wavelengths of both the pump and probe are varied, and a single decay is recorded at 90 °C. Fits to $A\exp(-t/T_2)\sin(\gamma B_0 t + \phi)$ extract amplitudes, which are plotted against probe tuning frequencies ν in steps of 0.73 GHz, and pump tuning plots vary by color from purple to red, in steps of 1.46 GHz (Fig. 2). When tuned directly on $F = 2$ ground-state transitions, the linearly polarized probe is heavily absorbed and undergoes no optical rotation, leaving near-zero signal amplitude. For the mid (○) regime, we have probe tuning $\nu = -6$ GHz providing a moderate optical rotation signal, with pumping tuned to the $F = 1$ ground-state transitions. When the probe is tuned to 4.27 GHz, there is an effective mechanism to depopulate the $F = 1$ manifold to the $F = 2$ ground states, such that a pump tuned to −2.56 GHz transitions from the $F = 2$ states results in near unity polarization in the $F = 2$ manifold, as denoted by (⋆). Because the probe is already detuned by 6.8 GHz from $F = 2$, we also achieve high optical rotation and low probe broadening for detection. When the pump was tuned to $F = 1$ at 4.27 GHz, a probe also tuned for $F = 1$ states counteracts any optical pumping to the $F = 2$ manifold, resulting in suppression (×) of signal. The response to laser tuning is robust with flipping pump light helicity and field, and remained similar across a range of Earth-scale fields (5–150 μT). To confirm cell pressures, the incident linearly polarized probe power is decreased to 0.5 mW, and transmission converted to absorption cross section $\sigma(\nu)$ by $I = I_0\exp[-n\sigma(\nu)l]$, with I/I_0 the output/input light intensity, number density n, and $l = 6$ mm path length through cell (Fig. 2 Inset). The absorption cross section $\sigma(\nu)$ is fit to four Voigt profiles, for each hyperfine ground to excited transition, giving a pressure broadening of $\Gamma_B = 0.59 \pm 0.02$ GHz, for 25 ± 1 Torr of Ar:N_2 [44].

To demonstrate sensitivity, lasers are tuned for the probe-assisted depopulation pumping regime. The probe detection is split to detect the vapor cell top and bottom [45] and optical rotation signals are captured, shown in Fig. 3. The shot-to-shot repetition rate is 2 kHz, with a detection period of 0.4 ms for each shot and $T_2 = 0.33$ ms. Separate shots are fit to decaying sine waves using a nonlinear fitting routine, where magnetic fields are extracted by $B = \gamma/\omega$. The raw magnetometer performance of roughly 200 fT/$\sqrt{\text{Hz}}$ is limited by the Libbrecht-Hall supply noise, demonstrated by the roughly ×5 lower gradiometer sensitivity of 35.7 ± 0.3 ΔfT/$\sqrt{\text{Hz}}$ (injecting broadband noise of 1 nT/$\sqrt{\text{Hz}}$ indicates a gradiometer common mode rejection ratio of ∼3000). Gradiometry projects that a magnetometer formed from recombining the cell top and bottom has a sensitivity of 18 fT/$\sqrt{\text{Hz}}$. While other methods have sensitivities that degrade significantly above the Earth's field (see Refs. [10,34,41]), we observe no field dependence between 10 and 100 μT. Moreover, we retain high sensitivity with a large bandwidth using less than $\pi/4$ optical rotation. Achieving a higher bandwidth by means that do not degrade sensitivity is important

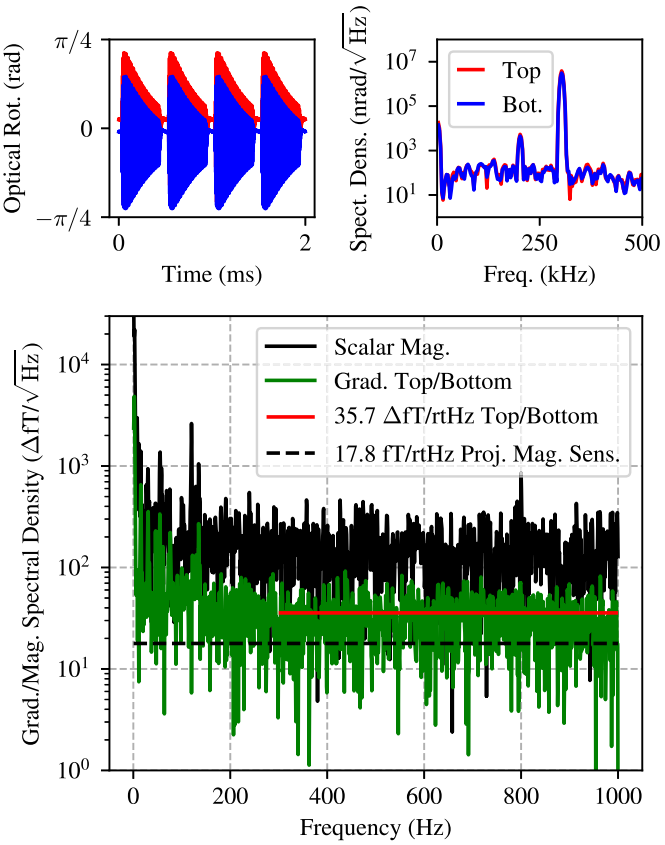

FIG. 3. Top/bottom optical rotation and spectral densities for 0.4-ms shots are shown. Frequencies are extracted for each shot for the vapor cell top/bottom, and repeated with 2 kHz. A probe-assisted depopulation pumping scalar magnetometer measures 44 μT with a current supply noise 200 fT/$\sqrt{\text{Hz}}$. Top/bottom gradiometry projects a magnetic field sensitivity of 17.8 ± 0.3 fT/$\sqrt{\text{Hz}}$ with a 1 kHz bandwidth.

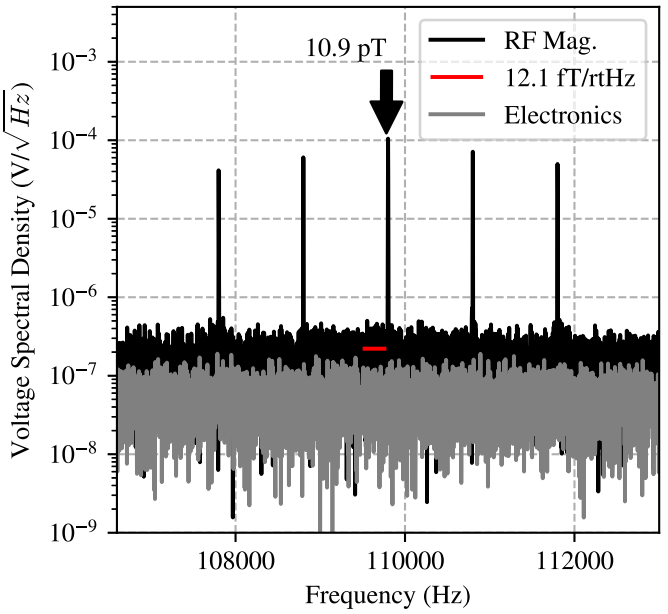

FIG. 4. An RF magnetometer is made with the same geometry as the scalar sensor, where the resonant frequency is determined by the 15.7 μT scalar field strength.

for gradient tolerance (and single-shot frequency error requirements), e.g., from Ref. [34], a similar cell size of 0.5 cm^3 with a high buffer gas, and multipass probe, yields 14 fT/$\sqrt{\text{Hz}}$ with a 90 Hz bandwidth—our 1 kHz bandwidth requires a factor of $\times 10$ less measurement time per shot. Here, gradient relaxation through diffusion is low compared to inhomogeneous T_2^* dephasing, so there is a proportional gain in gradient tolerance with decreasing measurement time $dB/dz = \Delta\phi/(\gamma L T)$, e.g., a signal height loss of $\text{sinc}(\Delta\phi) = 1/e$ results from 160 nT/cm over 0.4 ms, or 16 nT/cm in 4 ms. The measured gradiometer is higher than the Eq. (1) CRLB estimate of 27.2 fT/$\sqrt{\text{Hz}}$ for observed SNR and T_2, with a magnetometer of 13.6 fT/$\sqrt{\text{Hz}}$.

The same method and geometry can be used for RF magnetometry, which we show experimentally with the cell temperature increased to 130 °C and continuous probe-assisted depopulation pumping [16,46,47]. To calibrate test fields, the bias field B_0 is tuned for resonance near 110 kHz, and Rabi oscillations are driven within the rotating-wave approximation where the driving field B_1 is much less than B_0. In Fig. 4, we extract a magnetic field sensitivity of 12.1 ± 0.4 fT/$\sqrt{\text{Hz}}$. Five separate frequencies detected around 110 kHz are shown with an amplitude 10.9 pT, yielding a magnetometer full width at half maximum of roughly 3 kHz. The spin-projection noise limit is given by $\delta B = (1/\gamma)\sqrt{8/(F_z n V T_2)}$ where F_z is polarization along z, n is number density, and V is volume probed; for our parameters we find δB is below 10 fT/$\sqrt{\text{Hz}}$.

We demonstrated probe-assisted depopulation pumping for scalar and RF magnetometry in low buffer gas alkali-metal vapor cells. The small cell size and low-power, single-pass lasers used give an important proof of principle for compact, portable sensor heads using low-pressure vapor cells for improved gradient tolerance and retention of sensitivity in large Earth-scale fields. The suppression of hyperfine effects opens up a regime for precision magnetometry, including zerofield magnetometer extensions [48]; for example, a ^{87}Rb 50% polarized $F = 2$ manifold can be strongly probed with tuning at $F = 1$ ($\Delta\nu = 6.8$ GHz); here, the spin evolution due to a magnetic field will only have $F = 2$ character. In addition, this method is valid for the other popular alkali metals for precision magnetometry, K and Cs. To improve raw sensitivity, a multipass configuration may also be used, for spin-noise-limited operation [17,34,49–53].

We thank the Virginia Tech Office of Research and Innovation for support and Brian Saam for discussions.

DATA AVAILABILITY

The data that support the findings of this article are not publicly available upon publication because it is not technically feasible and/or the cost of preparing, depositing, and hosting the data would be prohibitive within the terms of this research project. The data are available from the authors upon reasonable request.

[1] H. Dang, A. C. Maloof, and M. V. Romalis, Ultrahigh sensitivity magnetic field and magnetization measurements with an atomic magnetometer, Appl. Phys. Lett. **97**, 151110 (2010).

[2] J. Kitching, Chip-scale atomic devices, Appl. Phys. Rev. **5**, 031302 (2018).

[3] C. N. Johnson, P. D. D. Schwindt, and M. Weisend, Multi-sensor magnetoencephalography with atomic magnetometers, Phys. Med. Biol. **58**, 6065 (2013).

[4] E. Boto, N. Holmes, T. M. Tierney, J. Leggett, R. Hill, S. Mellor, G. Roberts, G. Barnes, R. Bowtell, M. Brookes, *et al.*, Magnetoencephalography using optically pumped magnetometers, in *Fifty Years of Magnetoencephalography* (Oxford University Press, New York, 2020), p. 104.

[5] O. Alem, K. J. Hughes, I. Buard, T. P. Cheung, T. Maydew, A. Griesshammer, K. Holloway, A. Park, V. Lechuga, C. Coolidge, M. Gerginov, E. Quigg, A. Seames, E. Kronberg, P. Teale, and S. Knappe, An integrated full-head opm-meg system based on 128 zero-field sensors, Front. Neurosci. **17**, 1190310 (2023).

[6] J. C. Allred, R. N. Lyman, T. W. Kornack, and M. V. Romalis, High-sensitivity atomic magnetometer unaffected by spin-exchange relaxation, Phys. Rev. Lett. **89**, 130801 (2002).

[7] W. Happer and A. C. Tam, Effect of rapid spin exchange on the magnetic-resonance spectrum of alkali vapors, Phys. Rev. A **16**, 1877 (1977).

[8] W. Lee, V. G. Lucivero, M. V. Romalis, M. E. Limes, E. L. Foley, and T. W. Kornack, Heading errors in all-optical alkali-metal-vapor magnetometers in geomagnetic fields, Phys. Rev. A **103**, 063103 (2021).

[9] D. P. Hewatt, M. Ellmeier, C. Kiehl, T. S. Menon, J. W. Pollock, C. A. Regal, and S. Knappe, Investigating the hyperfine systematic error and relative phase in low-spin-polarization alkali-metal free-induction-decay magnetometers, Phys. Rev. A **111**, 033106 (2025).

[10] M. E. Limes, E. L. Foley, T. W. Kornack, S. Caliga, S. McBride, A. Braun, W. Lee, V. G. Lucivero, and M. V. Romalis, Portable magnetometry for detection of biomagnetism in ambient environments, Phys. Rev. Appl. **14**, 011002(R) (2020).

[11] R. J. Clancy, V. Gerginov, O. Alem, S. Becker, and S. Knappe, A study of scalar optically-pumped magnetometers for use in magnetoencephalography without shielding, Phys. Med. Biol. **66**, 175030 (2021).

[12] D. Sheng, A. R. Perry, S. P. Krzyzewski, S. Geller, J. Kitching, and S. Knappe, A microfabricated optically-pumped magnetic gradiometer, Appl. Phys. Lett. **110**, 031106 (2017).

[13] V. Gerginov, S. Krzyzewski, and S. Knappe, Pulsed operation of a miniature scalar optically pumped magnetometer, J. Opt. Soc. Am. B **34**, 1429 (2017).

[14] A. R. Perry, M. D. Bulatowicz, M. Larsen, T. G. Walker, and R. Wyllie, All-optical intrinsic atomic gradiometer with sub-20 ft/cm/$\sqrt{}$Hz sensitivity in a 22 μT earth-scale magnetic field, Opt. Express **28**, 36696 (2020).

[15] V. Gerginov, M. Pomponio, and S. Knappe, Scalar magnetometry below 100 FT/HZ$^{1/2}$ in a microfabricated cell, IEEE Sens. J. **20**, 12684 (2020).

[16] I. M. Savukov, S. J. Seltzer, M. V. Romalis, and K. L. Sauer, Tunable atomic magnetometer for detection of radio-frequency magnetic fields, Phys. Rev. Lett. **95**, 063004 (2005).

[17] S. Li, P. Vachaspati, D. Sheng, N. Dural, and M. V. Romalis, Optical rotation in excess of 100 rad generated by rb vapor in a multipass cell, Phys. Rev. A **84**, 061403(R) (2011).

[18] D. Sheng, S. Li, N. Dural, and M. V. Romalis, Subfemtotesla scalar atomic magnetometry using multipass cells, Phys. Rev. Lett. **110**, 160802 (2013).

[19] V. G. Lucivero, W. Lee, M. E. Limes, E. L. Foley, T. W. Kornack, and M. V. Romalis, Femtotesla nearly-quantum-noise-limited pulsed gradiometer at earth-scale fields, Phys. Rev. Appl. **18**, L021001 (2022).

[20] D. Hunter, M. S. Mrozowski, A. McWilliam, S. J. Ingleby, T. E. Dyer, P. F. Griffin, and E. Riis, Optical pumping enhancement of a free-induction-decay magnetometer, J. Opt. Soc. Am. B **40**, 2664 (2023).

[21] E. Alexandrov, M. Balabas, V. Kulyasov, A. Ivanov, A. Pazgalev, J. Rasson, A. Vershovski, and N. Yakobson, Three-component variometer based on a scalar potassium sensor, Meas. Sci. Technol. **15**, 918 (2004).

[22] A. Vershovskii, M. Balabas, A. Ivanov, V. Kulyasov, A. Pazgalev, and E. Aleksandrov, Fast three-component magnetometer-variometer based on a cesium sensor, Tech. Phys. **51**, 112 (2006).

[23] T. Wang, W. Lee, M. Limes, T. Kornack, E. Foley, and M. Romalis, Pulsed vector atomic magnetometer using an alternating fast-rotating field, Nat. Commun. **16**, 1374 (2025).

[24] C. Ottinger, R. Scheps, G. York, and A. Gallagher, Broadening of the rb resonance lines by the noble gases, Phys. Rev. A **11**, 1815 (1975).

[25] M. D. Rotondaro and G. P. Perram, Collisional broadening and shift of the rubidium D_1 and D_2 lines ($5^2S_{12} \rightarrow 5^2P_{12}, 5^2P_{32}$) by rare gases, H_2, D_2, N_2, CH_4, and CF_4, J. Quant. Spectrosc. Radiat. Transfer **57**, 497 (1997).

[26] M. V. Romalis, E. Miron, and G. D. Cates, Pressure broadening of rb D_1 and D_2 lines by ^{3}He, ^{4}He, N_2, and Xe: Line cores and near wings, Phys. Rev. A **56**, 4569 (1997).

[27] M. Erhard, S. Nußmann, and H. Helm, Power broadening and doppler effects of coherent dark resonances in Rb, Phys. Rev. A **62**, 061802(R) (2000).

[28] W. Happer, Y.-Y. Jau, and T. Walker, *Optically Pumped Atoms* (Wiley, Hoboken, NJ, 2010).

[29] G. Oelsner, R. IJsselsteijn, T. Scholtes, A. Krüger, V. Schultze, G. Seyffert, G. Werner, M. Jäger, A. Chwala, and R. Stolz, Integrated optically pumped magnetometer for measurements within earth's magnetic field, Phys. Rev. Appl. **17**, 024034 (2022).

[30] W. Happer and B. Mathur, Off-resonant light as a probe of optically pumped alkali vapors, Phys. Rev. Lett. **18**, 577 (1967).

[31] J. S. Bennett, B. E. Vyhnalek, H. Greenall, E. M. Bridge, F. Gotardo, S. Forstner, G. I. Harris, F. A. Miranda, and W. P. Bowen, Precision magnetometers for aerospace applications: A review, Sensors **21**, 5568 (2021).

[32] C. Abel, S. Afach, N. J. Ayres, G. Ban, G. Bison, K. Bodek, V. Bondar, E. Chanel, P.-J. Chiu, C. B. Crawford, Z. Chowdhuri, M. Daum, S. Emmenegger, L. Ferraris-Bouchez, M. Fertl, B. Franke, W. C. Griffith, Z. D. Grujić, L. Hayen, V. Hélaine, *et al.*, Optically pumped Cs magnetometers enabling a high-sensitivity search for the neutron electric dipole moment, Phys. Rev. A **101**, 053419 (2020).

[33] R. J. Hoare, E. R. Oteiza, and T. E. Chupp, The search for a permanent electric dipole moment using ^{129}Xe and ^{3}He, AIP Conf. Proc. **275**, 73 (1993).

[34] V. G. Lucivero, W. Lee, N. Dural, and M. V. Romalis, Femtotesla direct magnetic gradiometer using a single multipass cell, Phys. Rev. Appl. **15**, 014004 (2021).

[35] M. Limes, N. Dural, M. Romalis, E. Foley, T. Kornack, A. Nelson, and L. Grisham, Long spin-1/2 noble gas coherence times in mm-sized anodically bonded batch-fabricated ^{3}He-^{129}Xe-^{87}Rb cells, Appl. Phys. Lett. **126**, 134001 (2025).

[36] M. E. Limes, L. Rathbun, E. Foley, T. Kornack, Z. Hainsel, and A. Braun, Frequency-dependent amplitude correction to free-precession scalar magnetometers, IEEE Sensors Letters **9**, 1 (2025).

[37] N. Wilson, C. Perrella, R. Anderson, A. Luiten, and P. Light, Wide-bandwidth atomic magnetometry via instantaneous-phase retrieval, Phys. Rev. Res. **2**, 013213 (2020).

[38] A. Jaufenthaler, T. Kornack, V. Lebedev, M. E. Limes, R. Körber, M. Liebl, and D. Baumgarten, Pulsed optically pumped magnetometers: Addressing dead time and bandwidth for the unshielded magnetorelaxometry of magnetic nanoparticles, Sensors **21**, 1212 (2021).

[39] T. McClelland, L. K. Lam, and T. M. Kwon, Anomalous narrowing of magnetic-resonance linewidths in optically pumped alkali-metal vapors, Phys. Rev. A **33**, 1697 (1986).

[40] J. M. Dreiling, E. B. Norrgard, D. Tupa, and T. J. Gay, Transverse measurements of polarization in optically pumped rb vapor cells, Phys. Rev. A **86**, 053416 (2012).

[41] R. Zhang, D. Kanta, A. Wickenbrock, H. Guo, and D. Budker, Heading-error-free optical atomic magnetometry in the earth-field range, Phys. Rev. Lett. **130**, 153601 (2023).

[42] M. A. Rosenberry, J. P. Reyes, D. Tupa, and T. J. Gay, Radiation trapping in rubidium optical pumping at low buffer-gas pressures, Phys. Rev. A **75**, 023401 (2007).

[43] K. Libbrecht and J. L. Hall, A low-noise high-speed diode laser current controller, Rev. Sci. Instrum. **64**, 2133 (1993).

[44] M. Arditi and T. Carver, Hyperfine relaxation of optically pumped Rb^{87} atoms in buffer gases, Phys. Rev. **136**, A643 (1964).

[45] I. K. Kominis, T. W. Kornack, J. C. Allred, and M. V. Romalis, A subfemtotesla multichannel atomic magnetometer, Nature (London) **422**, 596 (2003).

[46] I. Savukov, T. Karaulanov, and M. G. Boshier, Ultra-sensitive high-density Rb-87 radio-frequency magnetometer, Appl. Phys. Lett. **104**, 023504 (2014).

[47] R. J. Cooper, D. W. Prescott, P. Matz, K. L. Sauer, N. Dural, M. V. Romalis, E. L. Foley, T. W. Kornack, M. Monti, and J. Okamitsu, Atomic magnetometer multisensor array for rf interference mitigation and unshielded detection of nuclear quadrupole resonance, Phys. Rev. Appl. **6**, 064014 (2016).

[48] A. Berrebi, M. Dikopoltsev, O. Katz, and O. Katz, Optical protection of alkali-metal atoms from spin relaxation, Phys. Rev. Lett. **135**, 023201 (2025).

[49] M. Romalis and T. Kornack, Scalar multi-pass atomic magnetometer, Air Force Research Laboratory Technical Report No. AFRL-RY-WP-TR-2017-0124 (2017), https://apps.dtic.mil/sti/tr/pdf/AD1037951.pdf

[50] Y. Liu, X. Peng, H. Wang, B. Wang, K. Yi, D. Sheng, and H. Guo, Femtotesla ^{4}He magnetometer with a multipass cell, Opt. Lett. **47**, 5252 (2022).

[51] S.-Q. Liu, Q.-Q. Yu, H. Zhou, and D. Sheng, Sensitive and stable atomic vector magnetometer to detect weak fields using two orthogonal multipass cavities, Phys. Rev. Appl. **19**, 044062 (2023).

[52] K. Yi, Y. Liu, B. Wang, W. Xiao, D. Sheng, X. Peng, and H. Guo, Free-induction-decay ^{4}He magnetometer using a multipass cell, Phys. Rev. Appl. **22**, 014084 (2024).

[53] D. J. Heilman, K. L. Sauer, D. W. Prescott, C. Z. Motamedi, N. Dural, M. V. Romalis, and T. W. Kornack, Large-scale multipass two-chamber rf atomic magnetometer, Phys. Rev. Appl. **22**, 054024 (2024).